PNAS RESEARCH ARTICLE | APPLIED PHYSICAL SCIENCES

# Reflection and refraction of directrons at the interface

Xing-Zhou Tang[a,b,1], Chao-Yi Li[a,c,1], Zhi-Jun Huang[a,1], Jia-Hui Zhao[a], Yu-Xi Chen[b], Nicholas L. Abbott[d], Juan J. de Pablo[b,e,f,2], Yan-Qing Lu[c,2], and Bing-Xiang Li[a,c,2]

Affiliations are included on p. 9.

Edited by Igor Muševič, Institut Jozef Stefan, Ljubljana, Slovenia; received January 21, 2025; accepted May 7, 2025 by Editorial Board Member Daan Frenkel

**Reflection and refraction are ubiquitous phenomena with extensive applications, yet minimizing energy loss and information distortion during these processes remains a significant challenge. This study examines the behavior of structurally stable solitons, known as directrons, in nematic liquid crystals interacting with an interface where the director field orientation changes, despite identical physical properties, external potentials, and boundary anchoring in the two regions. During reflection and refraction, the directrons maintain nearly constant structure and velocity, ensuring energy conservation and information integrity. Microscopic analyses of the director field and macroscopic evaluations of effective potential are employed to elucidate the dependence of reflection and refraction probabilities on the directron's incident angle and the orientation difference across the interface. The findings provide valuable insights into the dynamics of solitary waves in structured liquid crystal systems, offering significant implications for the development of tunable photonic devices, reconfigurable optical systems, and nanoscale material engineering.**

liquid crystal | dissipative soliton | interaction with interfaces

## Significance

This work achieves the refraction and reflection of flexoelectric-induced directrons at interfaces. With identical physical properties of the media on both sides of the interface, as well as uniform external fields and boundary anchoring energies, the structural soliton maintains consistent structure and speed before and after interaction with the interface, ensuring the integrity of the information. The study provides precise control over the incident angle and the molecular alignment distributions in both regions, enabling the modulation of both reflection and refraction phenomena and accurate adjustment of the refraction angle. This work opens up possibilities for the manipulation of information in soft matter systems and enhances the potential for advanced optical and photonic applications.

When waves propagate to the interface of heterogeneous media, reflection and refraction phenomena arising from differences in physical properties have long been fundamental topics in research (1–8). One of the most significant applications lies in information transformation. Solitons have been engineered for the long-distance propagation of optical signals and have been observed in liquid crystals (LCs) as either domain interfaces in the presence of rotating magnetic fields (9–14) or as localized director perturbations generated and propagated under a delocalized alternating current (AC) electric field (1, 15–26). The latter approach offers a promising method to harvest the energy of a delocalized field and focus it into micron-sized packets (19, 22, 25, 27), with potential applications in information or cargo transport, energy transduction through liquid–liquid interfaces (28), and the design of LC-based autonomous and adaptable microsystems (27, 29–31). When solitons traverse an interface, their motion may undergo changes due to differences in external fields (32) or boundary anchoring energies on either side of the interface (28).

From a physical perspective, the formation mechanism of liquid crystal solitons bears a profound analogy to that of classical optical solitons. Optical solitons maintain waveform stability through a dynamic balance between self-phase modulation and group velocity dispersion, whereas the stability of liquid crystal solitons arises from the interplay between elastic deformation energy and external field-driven forces. The director field of nematic liquid crystals is protected by the homotopy group $\pi_2\left(\frac{\mathbb{S}^2}{\mathbb{Z}_2}\right)$, reflecting the symmetry around a nematic axis, where each director orientation $\mathbf{n}(r)$ is equivalent to $-\mathbf{n}(r)$. If the liquid crystal possesses chirality, these solitons may exhibit topological stability, resembling "knots" that are difficult to untie and, therefore, resistant to dissipation. The topological stability leads to the formation of various topological solitons (24, 33–36). While most topological solitons exhibit stable structures, their limited mobility poses challenges for high-speed information transmission, despite their potential applications in information storage.

In nonchiral liquid crystals, the formation of solitons primarily depends on local director field variations (such as splay and bend) induced by external electric fields. Li et al. (18, 26) detailed the electrically driven solitons, termed "directrons," where dielectric polarization and flexoelectric polarization drive the director field to align either perpendicular or parallel to the field direction. The competition between these polarizations and the boundary conditions results in the formation of localized, stable, nontopological structures capable of propagating at relatively high speeds in a specific direction. Subsequent studies explored the phase diagram of solitons under varying electric field conditions and

Author contributions: N.L.A., J.J.d.P., Y.-Q.L., and B.-X.L. designed research; X.-Z.T., C.-Y.L., and Z.-J.H. performed research; X.-Z.T., C.-Y.L., Z.-J.H., J.-H.Z., and Y.-X.C. analyzed data; and X.-Z.T., C.-Y.L., Z.-J.H., N.L.A., J.J.d.P., Y.-Q.L., and B.-X.L. wrote the paper.

The authors declare no competing interest.

This article is a PNAS Direct Submission. I.M. is a guest editor invited by the Editorial Board.

[1] X.-Z.T., C.-Y.L., and Z.-J.H. contributed equally to this work.

[2] To whom correspondence may be addressed. Email: depablo@uchicago.edu, yqlu@nju.edu.cn, or bxli@njupt.edu.cn.

This article contains supporting information online at https://www.pnas.org/lookup/suppl/doi:10.1073/pnas.2501488122/-/DCSupplemental.

elucidated the physical mechanisms underlying soliton formation and propagation (21, 28, 30). These investigations achieved precise spatial and directional control over soliton generation and examined soliton transitions between regions with distinct physical properties, unveiling dynamic behaviors (1, 19, 22, 28, 32, 37, 38).

In this work, we employ photoalignment technology to customize the director orientations and define the interface regions and alignment directions (37, 39–41). When a directron encounters an interface, the likelihood of refraction increases as the director field at the point of contact becomes more aligned with the interface's orientation. Conversely, a larger mismatch in the local director field tends to favor reflection. At intermediate alignment, both reflection and refraction are possible, with the specific outcome determined by the timing of the interaction. This study demonstrates that by precisely controlling the background director distribution, it is possible to manipulate the trajectories of directrons and adjust the probabilities of reflection and refraction without altering the medium's material properties or boundary anchoring conditions.

The directrons exhibit stable morphology, long travel distances, controllable trajectories, and a wide range of tunable motion. The findings of this study highlight the application potential of directrons in information transmission. Maintaining consistency in material parameters effectively ensures the morphological integrity and velocity consistency of the information carrier. The reconfigurable interface allows for reversible modification without compromising system stability. These characteristics establish directrons as soft-matter information carriers with long-range transport capabilities, programmable trajectories, and seamless interfacial transitions.

## Results and Discussion

**Research Design and Phenomena.** When directrons approach and interact with interfaces, reflection and refraction are observed. The directrons are generated by applying an AC electric field to a nematic liquid crystal with negative dielectric anisotropy. The causes and analyses of directron generation and motion are discussed in the Supplementary Information (*SI Appendix, Text 1*). Photoalignment technology (*SI Appendix, Text 2*) allows precise control over the interface by designing the director orientations on both sides. As shown in Fig. 1*A*, a UV-polarization-sensitive sulfonic azo-dye SD1 is coated on the glass substrates and exposed at a designated wavelength, 405 nm. A designed background alignment is achieved, and 4'-butyl-4-heptyl-bicyclohexyl-4-carbonitrile (CCN-47) is introduced into the NLC cells. The AC field is oriented perpendicular to the liquid crystal cell ($z$-direction), causing the directrons to propagate predominantly perpendicular to the director. The material properties, boundary anchoring strength, and applied electric field are identical on both sides of the interface. The applied voltage ranges from 40 to 80 V, with frequencies varying between 500 and 800 Hz.

With the designed boundary alignment established by photoalignment, the bulk liquid crystals spontaneously reorient to match these boundary conditions, naturally forming a distinct interface. Consequently, the interface position and the director orientations on each side are precisely determined by the patterned surface alignment. The director fields in both regions are represented as $\boldsymbol{n}_1$ and $\boldsymbol{n}_2$, which is detailed in *SI Appendix*, Fig. S3. The angle between the regions is defined as $\beta_1 = \frac{\boldsymbol{n}_1 \cdot \boldsymbol{n}_2}{|\boldsymbol{n}_1 \cdot \boldsymbol{n}_2|}$, and the angle between the top region and the $+x$ direction is defined as $\beta_2 = \frac{\boldsymbol{n}_1 \cdot \hat{\boldsymbol{x}}}{|\boldsymbol{n}_1|}$. Fig. 1*B* shows the full waveplate polarizing optical microscope (POM) image in the absence of an AC field. Here, **A** refers to the analyzer's direction, and **P** refers to the polarizer's direction, which are orthogonal. The aligned directors appear as a deep red background, with the slow axis ($\lambda$) represented by rods oriented at 45° to the crossed polarizer. Directrons propagate perpendicular to the director field, inducing local color variations that indicate their direction (Fig. 1*C*). To ensure clear observation of reflection and refraction, the interfacial director orientations differ by 91°, with a 1° perturbation added to prevent overlap between reflected and incident trajectories at normal incidence.

Fig. 1*D* presents the observed refraction and reflection phenomena at a fixed interfacial angle of 91°. Both regions appear deep red due to alignment with the analyzer or polarizer directions. The interface, aligned along the x-axis, exhibits a clockwise gradient, appearing yellow. The incident angles ($\theta$) of 66°, 0°, −10°, and −76° are shown from left to right, with counterclockwise angles defined as positive and clockwise as negative (see *SI Appendix*, Fig. S4 for details). At incident angles of 66° and −76°, directrons can traverse the interface, exhibiting refraction. Both the incident and refracted angles are on the same side of the normal, resulting in negative refraction. It is observed that directrons travel perpendicularly to the director fields in both uniformly aligned regions, with their yellow and green wings switching upon crossing the interface due to the angular difference in director orientations on either side. At incident angles of 0° and − 10°, reflection occurs, with the reflected angles at − 10° being negative, indicating negative reflection. Before and after reflection, the colors of the director wings also switch, demonstrating that the directron's direction of motion reverses.

The orientation difference $\beta_1$ between the director orientations in the two regions can also be precisely controlled using photoalignment technology. Fig. 1*E* shows the scenario where the angle between the upper region's director orientation and the $x$-axis is fixed at $\beta_2 = 0°$, and directrons are incident from regions with different $\beta_1$ values of 130°, 155°, 25°, and 60°. Throughout the process of directrons entering the $\boldsymbol{n}_2$ region from the $\boldsymbol{n}_1$ region, they consistently move perpendicular to the director orientations. Since the angle between the two regions is not perpendicular, the color of directrons in the $\boldsymbol{n}_2$ region does not always appear yellow and green. The background color of the lower region varies among yellow, green, and red based on the orientation of $\boldsymbol{n}_2$. The clockwise or counterclockwise transition of the director orientation across the interface can result in yellow and green regions. This study allows precise adjustment of the interface position and angle, as well as the alignment of directors in both regions, $\beta_1$ and $\beta_2$, enabling flexible control over directron motion modes, including refraction, reflection, and various exit angles. The detailed process of the directrons in various times of Fig. 1 *D* and *E* is shown in *SI Appendix*, Figs. S8 and S9.

**Modulation of Incident Angles.** By fixing the orientation difference $\beta_1$ between the directors of the two regions and varying the incident angles, different reflection and refraction behaviors can be observed. Fig. 2*A* illustrates the reflection and refraction phenomena at various $\beta_2$ under 7.25 V and 800 Hz. During refraction, the propagation orientation remains perpendicular to the background director field. However, during reflection, there is a noticeable difference between the incident and reflected angles, especially at larger incident angles, where the difference becomes more significant. Refraction can be understood as the directron gradually changing its direction of motion within differently aligned director fields until it resumes linear motion

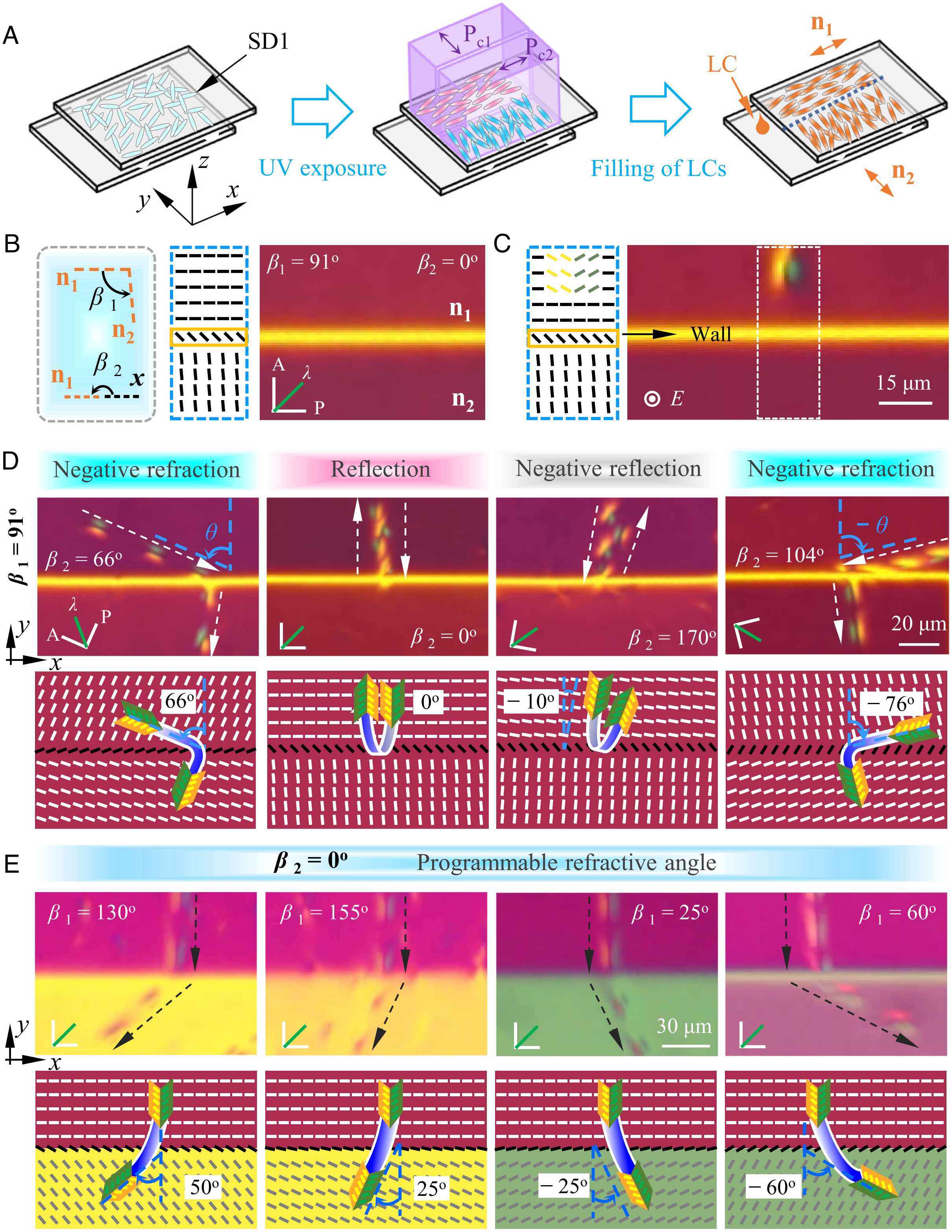

**Fig. 1.** Schematic of preparation of the binary pattern utilizing the photoalignment technique based on a digital-micro-mirror device. (*A*) Fabrication process of the NLC sample. Blue arrows represent the linear polarization of UV light. (*B*) Polarizing optical microscope (POM) figure captured at the absence of electric fields, presented with a full waveplate (530 nm). $\beta_1$ is the angle between directors within *Upper* and *Bottom* regions. $\beta_2$ is the angle between *x*-axis and $n_1$. (*C*) Illustration of directrons' generation by applying an AC field onto an NLC cell. (*D*) Interactions between solitons and interfaces when $\beta_1$ is fixed at 91°. (*E*) Programmable refraction angle by manipulating $\beta_1$ when $\beta_2$ is fixed at 0°.

in a uniformly aligned region. In contrast, reflection resembles a strong interaction between the directron and the interface, where the incident directron alters the interface's morphology, creating an extra directron source on the same side as the incident directron but moving in the opposite direction. The interaction between the incident directron and the interface modifies the director orientations near the collision point, causing the reflected directron to deviate in its direction of motion. In certain cases, directrons can also be absorbed by the interface. The probability of absorption is low in this study because the electric field conditions

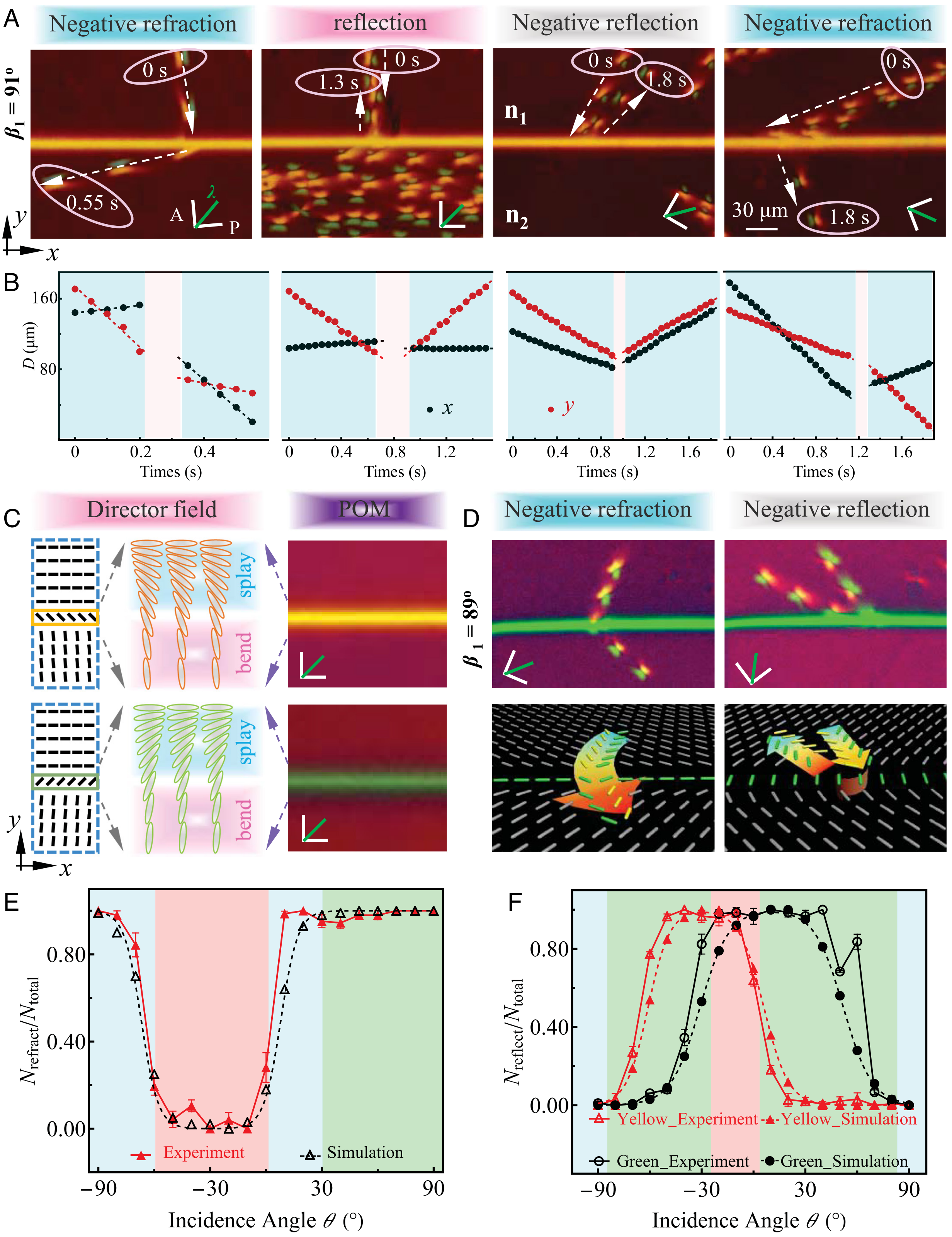

**Fig. 2.** Investigation on interactions between solitons and walls when $\beta_1$ is fixed at either 91° or 89°. (*A*) Negative reflection, negative refraction, and total reflection occur after the interaction between solitons and interfaces. (*B*) Time dependence of the $x$- and $y$-coordinates of solitons for different situations. (*C*) Director field and POM textures of yellow ($\beta_1 = 91°$) and green walls ($\beta_1 = 89°$), displayed with a full waveplate (530 nm). (*D*) Negative reflection and negative refraction for green interfaces. (*E*) Statistics and corresponding simulation results of refraction during the interaction between solitons and yellow boundaries. (*F*) Statistics and corresponding simulation results of reflection when solitons interact with yellow and green boundaries, respectively.

are set such that the length of directrons exceeds the width of interfaces, ensuring that most directrons either reflect or refract. Fig. 2*B* shows detailed directron trajectories, indicating that before and after interacting with the interface, directrons maintain uniform linear motion with minimal changes in velocity and size, demonstrating that energy loss during interaction is negligible and the directron's structural information remains largely unchanged. As mentioned earlier, when the director orientations transition differently across the interface, the POM images display yellow and green colors, as shown in Fig. 2*C*. The upper region's director orientation $\boldsymbol{n}_1$ is primarily aligned along the $x$-direction, while the lower region's $\boldsymbol{n}_2$ is aligned along the $y$-direction. At the interface, the upper part shows expansion or conversion on the plane that perpendicular to the nematic axis, exhibits splay deformation, and the lower part represents angular difference along the nematic axis, shows bend deformation. If the angle between the interface center and the $x$-axis is $+45°$, it appears yellow; conversely, $-45°$ corresponds to green. More refraction and reflection cases with various indicate angles for fixed $\beta_1$ are shown in *SI Appendix*, Figs. S5 and S6.

Green interfaces also exhibit reflection and refraction phenomena. Fig. 2*D* shows two interaction processes occurring at green interfaces. In Fig. 2*C*, the green and yellow interfaces are mirror images of each other; the yellow interface results from a clockwise rotation of the director field from top to bottom, while the green interface is formed by a counterclockwise rotation, with the corresponding $\beta_1$ being $-89°$. The schematic below illustrates the background, interface, and director distribution for each case. Reflection and refraction at green interfaces follow similar patterns to those at yellow interfaces: Directrons typically move perpendicular to the background director field, and during reflection, the exit angles deviate from the incident angles.

The reflection and refraction phenomena are closely related to the timing at which directrons collide with the interface. In practical experiments, precise timing control is challenging because the response time of the liquid crystal is typically one to two orders of magnitude longer than the period of the excitation voltage driving the directrons. Additionally, directrons approaching the interface interact with each other, altering their structures and velocities near the boundary. These combined effects introduce randomness into the reflection and refraction outcomes, making it difficult to predict whether a given directron will undergo reflection or refraction solely based on initial conditions. To quantitatively characterize this inherent variability, reflection and refraction events of 50 directrons were statistically analyzed over a specified time period.

Fig. 2*E* shows the reflection and refraction behavior at 7.25 V and 800 Hz. Directrons incident at $-60°$ to 0° (red region) primarily reflect, while those at 30° to 90° refract. At intermediate angles (blue region), both behaviors are possible. The 700 Hz. refraction rate is given in *SI Appendix*, Fig. S7. At large incident angles that result in refraction, the bend alignment direction matches the curvature of the directron head, minimizing energy changes and facilitating penetration. At other angles, significant director rearrangements (~90°) would be required for penetration, incurring prohibitive energy costs. Instead, directrons induce localized deformations at the interface, creating new directron sources.

Unlike the experimental randomness, theoretical simulations allow precise control over the timing of directron emission, enabling timed excitation through voltage modulation. To simulate experimental stochasticity, directrons were excited at different times within a single voltage cycle, with a time step of $0.01T$. The mechanisms ensuring timely emission of directrons and the outcomes of collisions at the interface under varying timing conditions are detailed in the Supplementary Information (*SI Appendix*, *Text 3*). A total of 100 simulations were conducted, and the proportions of reflected and refracted directrons were statistically analyzed. The corresponding voltage settings are detailed in the Materials and Methods section, where we also discuss the reflection and refraction events occurring within a single cycle, along with the dynamics of directron motion. The reflection and refraction rates obtained from numerical simulations are represented as dashed lines in Fig. 2 *E* and *F*.

For interfaces transitioning from the $\boldsymbol{n}_1$ to $\boldsymbol{n}_2$ region clockwise, as shown in the POM image with a green interface (Fig. 2*F*), under the same electric conditions as Fig. 2*E*, directrons passing through the yellow boundary with incident angles ranging from −65° to $-5°$ primarily undergo reflection. Under the same electric field conditions, directrons passing through the green boundary exhibit higher reflection rates for incident angles between −25° and 35°. Experimentally, it is observed that when the incident angle is between −25° and $-5°$, reflection always occurs regardless of the relative angle between the two regions (red region in the figure). In contrast, angles between −90° to −85° and $+85°$ to $+90°$ consistently result in refraction (blue region in the figure). The reflection rates in Fig. 2*F* are depicted with red and black lines, where solid lines represent experimental data and dashed lines represent theoretical simulations. It can be observed that the two lines intersect at an incident angle of $-15°$, and the reflection rates for green interfaces exhibit symmetry relative to yellow interfaces. When the director orientation at the center of the interface changes from $+45°$ to −45°, the reflection rate distribution undergoes a mirror-like transformation.

**Modulation of the Interface.** To investigate the phenomenon when the orientation difference between $\boldsymbol{n}_1$ to $\boldsymbol{n}_2$ is not 90°, this study maintains the angle $\beta_2$ between the director in the incident region and the $x$-axis while varying the orientation difference $\beta_1$ between the two regions. The study examines directron refraction and reflection under different conditions. Fig. 3*A* depicts the director deformation at the interface for different $\beta_1$ values, while Fig. 3*B* illustrates the reflection and refraction phenomena resulting from orientation differences between regions $|\beta_1|$. The directron trajectories are shown in Fig. 3*C*. The difference between the directron's incident and exit velocities is not large because the electric field conditions and surface anchoring energies in both regions are consistent. When $\beta_1$ varies between 0° and 180°, refraction is the most probable phenomenon, as the angular changes between regions are generally mild, presenting low obstruction to the directron. Only when the regions are about perpendicular to each other, reflecting appears. Fig. 3*D* shows trajectory maps for different exit angles over one second, and Fig. 3 *E* and *F* display the refraction rate under various $\beta_1$ conditions, based on experimental and numerical simulation results. When $\beta_1$ is between 45° and 135°, directrons may undergo either reflection or refraction, with the probability of refraction reaching its minimum at 90°. In all other cases, regardless of whether the interface color determined by the orientation difference is yellow or green, the observed phenomenon is almost exclusively refraction.

**Numerical Simulations and Mechanistic Analysis.** Numerical simulations accurately reproduce the experimentally observed phenomena. In previous experimental sections, we observed that under certain incident conditions, directrons predominantly undergo either reflection or refraction. Adjusting the relative orientations of two regions also influenced the exit angles of the director. Theoretical simulations, conducted under identical electric field conditions ($U = 78.5$ V, $f = 800$ Hz), corroborated these findings. Fig. 4*A* illustrates instances of reflection and refraction with fixed regional orientations, while Fig. 4*B* depicts changes in exit directions for $\beta_1$ angles

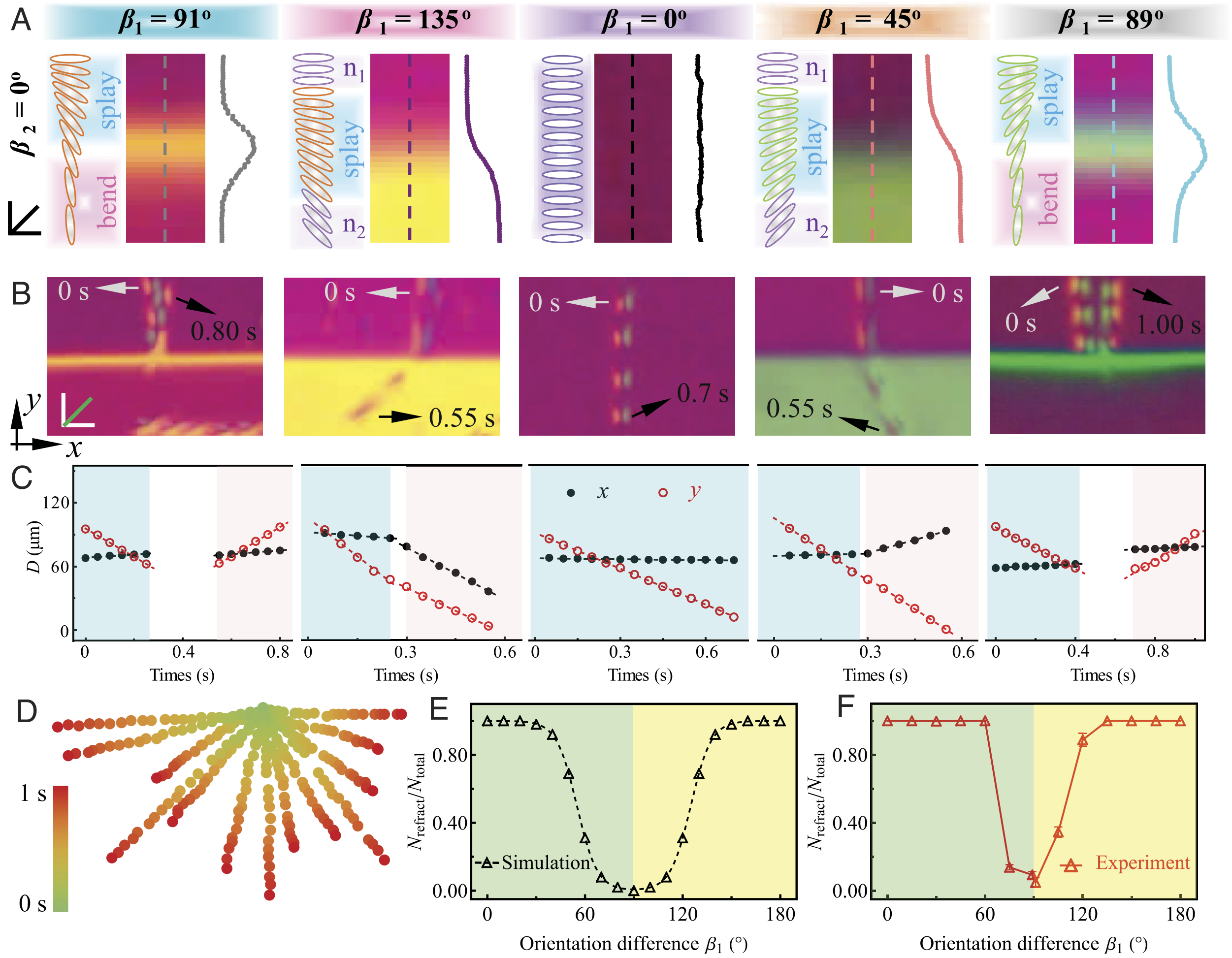

**Fig. 3.** Investigation on interactions between solitons and walls when $\beta_2$ is fixed at 0°. (*A*) Dependence of boundary morphology and its director distribution on $\beta_1$. Curves on the right side of the POM textures are corresponding intensity analysis of dotted lines. (*B*) Dependence of refraction on $\beta_1$. (*C*) Time dependence of the $x$- and $y$-coordinates of solitons. (*D*) Typical time-dependent trajectories of solitons during different motions at various $\beta_1$, stacked over 1 s. (*E*) Simulation outcomes corresponding to the experiments. (*F*) Statistics results of refraction when solitons interact with boundaries.

of 155° and 25°, respectively. The simulations align closely with experimental observations. The implementation of POM images in simulations is discussed in detail in the Supplementary Information (*SI Appendix*, *Text 4*).

Notably, in certain scenarios, directrons at the interface can undergo either refraction or reflection, a phenomenon linked to the timing of incidence. Fig. 4*C* presents the morphology of directrons at various moments within a voltage cycle, with Fig. 4 *D* and *E* detailing the temporal variations in light intensity and size. The length and width of the directron are defined based on the variation of light intensity; specifically, the boundary of a directron is determined at the position where the intensity decreases to 5% of its maximum value. Within a single voltage cycle, the directron's light intensity exhibits two peaks corresponding to the voltage extrema. At $t_1 = \eta T$ or $t_3 = \eta T + 0.5T (\eta = 1, 2, 3, \cdots)$, the light intensity diminishes, attributed to the correlation between the directron's *xy*-plane dimensions and voltage magnitude, given that the electric field term in the energy distribution is quadratic. The asymmetry between the peaks at $t_2 = \eta T + 0.25T$ and $t_4 = \eta T + 0.75T$ arises from the polarity introduced by the flexoelectric effect. At $t_2$, with the voltage directed along -$z$, the flexoelectric effect reduces splay and bend, rendering the directron's morphology closer to the nematic state, thereby slightly lowering the light intensity compared to $t_4$. This occurs because the electric field's influence on the director field is represented by $f_{\text{electric}} = -\frac{\varepsilon_0 \varepsilon_a}{2}(\boldsymbol{E} \cdot \mathbf{n})^2$, which is an even function of the voltage. Here, $\mathbf{n}$ is the director field of the LC, $\varepsilon_0$ is the vacuum permittivity, and $\varepsilon_a$ is the dielectric anisotropy. Both theory and experiment show slight differences between the two peaks within a cycle due to the flexoelectric effect, where the flexoelectric energy is given by $f_{\text{flexo}} = \frac{1}{2}\boldsymbol{E} \cdot \left[e_{11}\mathbf{n} \cdot (\nabla \cdot \mathbf{n}) - e_{33}\mathbf{n} \times \nabla \times \mathbf{n}\right]$, with $e_{11}$, and $e_{33}$ being the flexoelectric coefficients. This effect is an odd function of the electric field, resulting in the weakening or enhancement of light intensity depending on the field's polarity.

To elucidate the mechanisms underlying different directron behaviors, a macroscopic framework treating the directron as a particle was employed to analyze the effective potential in its vicinity. In our previous work, we established a "directron machine gun," which enables controlled generation of directrons from any designed position (37). This setup allows the theoretical study of directrons reaching the interface at designated times. Under a voltage of $U = 68.7\text{V}$ and a frequency of 500 Hz, the behaviors of directrons at different time points were investigated. Fig. 4*F* depicts five distinct cases. The first directron, highlighted with a red ring, appears at $t = 1.40\ \text{s} + 0.25\text{T}$, while the second, third, fourth, and fifth directrons, circled in green, purple, blue, and orange, respectively, occur at $t = 1.52\text{s} + 0.5\text{T}, 6.43\ \text{s} + 0.15\text{T}, 6.43\ \text{s} + 0.5\text{T}$, and $6.46\ \text{s} + 0.75\text{T}$.

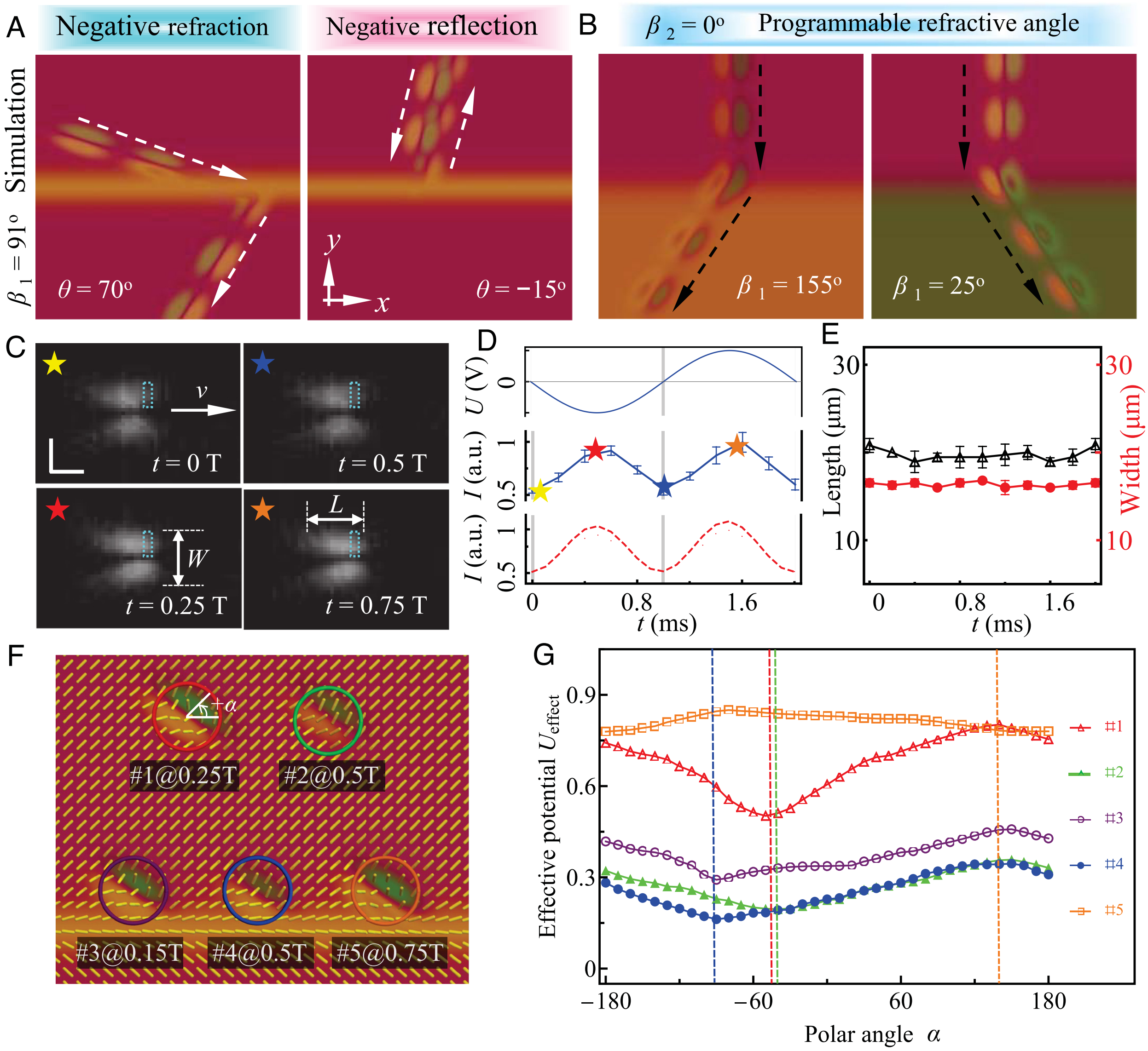

**Fig. 4.** Theoretical explanation of reflection and refraction. (*A*) Simulation outcomes corresponding to the interactions between solitons and interfaces when $\beta_1$ is fixed at 91°. (*B*) Simulation outcomes corresponding to the programmable refraction angle. (*C*) Images of directrons within one electric field cycle. (*D*) Experiment and simulation outcomes of the transmitted light intensity within one electric field cycle. (*E*) Experiment outcomes of the directrons's size within one electric field cycle. (*F*) Schematic diagram and (*G*) effective potential $U_{\mathrm{effect}}$ of the interaction between solitons and the interface.

Directrons 1 and 2 remain distant from the interface. Due to the negative dielectric anisotropy of CCN-47, the dielectric force and boundary conditions align the director field along the nematic principal axis. Flexoelectric effects induce bending of the director field along the electric field direction, creating stable bend and splay deformations perpendicular to the principal axis, which form propagating directrons. In contrast, directrons 3, 4, and 5 collide with the interface at different phases of the electric field cycle. Directron 3 interacts with the interface at $0.15T$ of the cycle, directron 4 at $0.5T$, and directron 5 at $0.75T$. Fig. 4*G* shows the effective potential density, $U_{\mathrm{eff}}$. The nematic order is described by the director field $\boldsymbol{n}(\boldsymbol{r}, t)$ coupled with the fluid flow velocity field $\boldsymbol{v}(\boldsymbol{r}, t)$, and the dissipate $D = \int d^3r\left[\frac{1}{2}\alpha_4 A_{ij}A_{ij} + \frac{1}{2}\gamma_1 N_i N_i\right]$ is composed by two modes: the strain rate tensor $A_{ij} = \frac{1}{2}(\partial_i v_j + \partial_j v_i)$ and the director rotation with respect to the background fluid vorticity $N_i = \dot{n}_i - \frac{1}{2}\epsilon_{km}\partial_k v_m \epsilon_{ji} n_j$, where $\epsilon$ is the Levi–Civita symbol. Around these directrons:

$$\begin{aligned} U_{\mathrm{eff}} &= f + \int dn_i \frac{\delta[D]}{\delta \dot{n}_i} \\ &= \frac{1}{2}As^2 + \frac{1}{3}Bs^3 + \frac{1}{4}Cs^4 + \frac{1}{2}(K_{11} - K_{24})(\nabla \cdot n)^2 \\ &+ \frac{1}{2}(K_{22} - K_{24})(n \cdot (\nabla \times n))^2 + \frac{1}{2}K_{33}|n \times (\nabla \times n)|^2 \\ &- K_{24}Tr(\Delta^2) - \frac{\varepsilon_0 \varepsilon_a}{2(E \cdot n)^2} \\ &- \frac{1}{2}E \cdot [e_{11} n \cdot (\nabla \cdot n) - e_{33} n \times (\nabla \times n)] + \int dn_i \frac{\delta[D]}{\delta \dot{n}_i} \end{aligned} \qquad [1]$$

Here, $s$ is the nematic order parameter, and $A$, $B$, and $C$ are Landau–de Gennes coefficients determining the nematic–isotropic transition. $\Delta$ is the biaxial splay (42–44), and $K_{11}$, $K_{22}$, $K_{33}$, and $K_{24}$ are the splay, twist, bend, and saddle-splay elastic constants. The coherence length of the directron is approximately $\xi_C = \sqrt{\frac{\left(\frac{B^2}{C}\epsilon_0\epsilon_\alpha E^2 + e_{11}|E|\right)}{K_{11}}} \approx 8$ μm.

The normalized effective potential reveals that directrons 1 and 2 exhibit higher potential energy at the tail compared to the head, with directron 1 experiencing larger mean energy and energy difference due to its interaction at a higher voltage phase, resulting in greater velocity. Directrons 3, 4, and 5 display distinct behaviors upon interface interaction. Directron 3, with its minimum $U_{\mathrm{eff}}$ at $-90°$, refracts into the third quadrant due to its energy gradient. Directron 4 has a smaller effective potential and energy variation, leading to low velocity and eventual absorption by the interface. Directron 5 exhibits a significant increase in $U_{\mathrm{eff}}$ at $-90°$ due to rapid director field changes, generating a repulsive force and causing reflection.

Microscopically, the head of the directron exhibits bend distortions that fluctuate with the electric field cycle. At higher voltages, the tangential bend component aligns more closely with the $x$-axis, while at lower voltages, it favors the $y$-axis. This results in an angular difference between the director at the head of the directron and the interface. Consequently, during a voltage cycle, higher voltages lead to a larger angle, generating a repulsive force that enables reflection, whereas lower voltages produce a smaller angle, facilitating refraction. At very low voltages, the interface's director field undergoes continuous changes with elevated elastic energy, making it difficult for the electric field to sustain the directron structure, leading to dissipation. Theoretical and numerical analyses successfully reproduce experimentally observed phenomena, providing insights into the mechanisms of refraction, reflection, and absorption at the interface.

## Conclusion

This study demonstrates that the interaction of directrons with interfaces in nematic liquid crystals is highly sensitive to the director distributions and interface geometry. By varying the incident angle of the directron and the relative orientation between regions, we observed cases where only reflection or refraction occurs, as well as scenarios where both phenomena are present, or the directron is absorbed by the interface. Theoretical and simulation analyses reveal that these behaviors arise from the interplay between microscopic director field variations and macroscopic effective potentials. Specifically, voltage-induced changes in the director field over one electric field cycle modulate the interaction dynamics at the interface, leading to distinct outcomes.

The findings underscore the critical role of the angular difference between director orientations in dictating refraction and reflection phenomena, enabling precise control of directron trajectories through customized interface designs. This work provides valuable insights into the dynamics of solitary waves in structured liquid crystal environments, with significant implications for tunable photonic devices, reconfigurable optical systems, and nanoscale material engineering. Future research could investigate the influence of more complex director configurations and external field variations to further enhance the applicability of directron–interface interactions in soft matter systems.

## Materials and Methods

**Materials.** A single-component liquid crystal, 4′-butyl-4-heptyl-bicyclo-hexyl-4-carbonitrile (CCN-47, Nematel GmbH), with negative dielectric and conductive anisotropies ($\Delta\varepsilon \sim -4.2$, $\Delta\sigma \sim -1.2 \times 10^{-9}\ \Omega^{-1}\ \mathrm{m}^{-1}$, at 45°C and 4 kHz), was used to generate directrons. This liquid crystal exhibits a nematic phase within a temperature range from 29. 9°C to 58. 5°C. The aligning layer, sulfuric azo-dye SD1 (Dai-Nippon Ink and Chemicals, Japan), facilitates photoreorientation when illuminated by linearly polarized UV light.

**Fabrication of the NLC Sample.** Glass substrates coated with indium-tin-oxide electrode were cleaned using ultrasonic bath (SERUTEX S-11, Nihon Measure) for 20 min and UV-Ozone bath for 30 min. To achieve the photoresponsive alignment layer, the substrates were coated with solution of 0.35 wt% SD1 in dimethylformamide (DMF, Sigma-Aldrich) at 800 rpm for 10 s and 3,000 rpm for 40 s using a spin processor WS-650Mz-23NPPB, Laurell. After heating on the hot stage for 10 min, pairs of substrates were assembled to form cells of thickness $d = 8.0 \pm 0.3\ \mu\mathrm{m}$ determined by the 8.0 μm-spacer-doped UV glue. The glue underwent the solidification after 2 min of UV irradiation ($\lambda = 405$ nm).

**Generation and Characterization of Directrons.** The generation of directrons was achieved by applying sinusoidal alternating voltages to the NLC cells using a signal generator (33522B, Keysight Technologies) and a signal amplifier (ATA-2081, Aigtek). The temperature of the NLC was controlled using the hot stage (LTS120E, Linkam). Videos and micrographs were recorded under a polarized optical microscope (50i POL, Nikon) using either a microscope camera (DS-Fi3, Nikon) or a high-speed camera (SH3-502, SSZN).

**Theoretical Framework.** To investigate the structural stability and dynamic behavior of directrons, the system was analyzed by minimizing the Frank–Oseen free energy density, incorporating contributions from dielectric coupling and flexoelectric effects under the applied electric field. The total free energy density is expressed as follows (30, 31, 45–47):

$$\begin{aligned} f_{\mathrm{NLC}} &= f_{\mathrm{LdG}} + f_{\mathrm{elastic}} + f_{\mathrm{electric}} + f_{\mathrm{flexo}} \\ &= \frac{1}{2}As^2 + \frac{1}{3}Bs^3 + \frac{1}{4}Cs^4 + \frac{K_{11}}{2}(\nabla\cdot\mathbf{n})^2 + \frac{K_{22}}{2}(\mathbf{n}\cdot\nabla\times\mathbf{n})^2 \\ &+ \frac{K_{33}}{2}(\mathbf{n}\times\nabla\times\mathbf{n}) - K_{24}\nabla\cdot[\boldsymbol{n}(\nabla\cdot\boldsymbol{n}) + \boldsymbol{n}\cdot(\nabla\times\boldsymbol{n})] - \frac{\varepsilon_0\varepsilon_{\mathrm{a}}}{2}(\mathbf{E}\cdot\mathbf{n})^2 \\ &+ \frac{1}{2}\mathbf{E}\cdot\left[e_{11}\mathbf{n}\cdot(\nabla\cdot\mathbf{n}) - e_{33}\mathbf{n}\times\nabla\times\mathbf{n}\right] \end{aligned}, \qquad [2]$$

where $\mathbf{n}$ is the director field of the LC, representing the molecular alignment; $K_{11}$, $K_{22}K_{33}$, and $K_{24}$ are the Frank elastic constants for splay, twist, bend, and saddle splay deformations, respectively; $\varepsilon_0$ is the vacuum permittivity; $\varepsilon_{\mathrm{a}}$ is the dielectric anisotropy; and $e_{11}$ and $e_{33}$ are the flexoelectric coefficients. The $K_{24}$ term is considered zero because the volume integral of the total derivative can be converted into a surface integral. Given that this study employs fixed boundary conditions with infinite anchoring, the surface integral remains constant and does not contribute to the dynamic equations.

The theoretical model employed for simulations aimed at explaining and exploring the complex behavior of directrons is based on the Landau–de Gennes free energy for liquid crystals. This model is described by the tensorial order parameter $\mathbf{Q}$. For uniaxial systems, $\mathbf{Q}$ can be written as $\mathbf{Q} = \mathrm{S}(\mathbf{nn} - \mathrm{I}/3)$, where $\mathbf{n}$ is the unit vector representing the nematic director field, and S is the largest eigenvalue of $\mathbf{Q}$ that quantifies the degree of uniaxial alignment. The tensorial order parameter evolves through the Ginzburg–Landau equation (48):

$$\frac{\partial}{\partial t}\mathbf{Q} = \Gamma\mathbf{H}, \qquad [3]$$

where the molecular field $\mathbf{H}$ is

$$\mathbf{H} = -\left(\frac{\delta\mathcal{F}}{\delta\mathbf{Q}} - \frac{\mathbf{I}}{3}\mathrm{Tr}\frac{\delta\mathcal{F}}{\delta\mathbf{Q}}\right). \qquad [4]$$

The free energy $\mathcal{F}$ of the system is defined within a phenomenological Landau–de Gennes framework:

$$F = \int_V \left[f_{\mathrm{LdG}} + f_{\mathrm{elas}} + f_{\mathrm{flex}} + f_{\mathrm{diel}}\right] dV + \int_{\partial V} f_{\mathrm{surf}}\, dS, \qquad [5]$$

where the total free energy $\mathcal{F}$ is composed of bulk contributions ($f_{\mathrm{LdG}}$, $f_{\mathrm{elas}}$, $f_{\mathrm{flex}}$, and $f_{\mathrm{diel}}$) and a surface interaction $f_{\mathrm{surf}}$ with the liquid crystal at the boundary.

The $f_{\mathrm{LdG}}$ term describes the isotropic–nematic phase transition:

$$f_{\mathrm{LdG}} = \frac{A_0}{2}\left(1 - \frac{\mathcal{U}}{3}\right)Tr\left(\boldsymbol{Q}^2\right) - \frac{A_0\mathcal{U}}{3}Tr\left(\boldsymbol{Q}^3\right) + \frac{A_0\mathcal{U}}{4}\left(Tr\left(\boldsymbol{Q}^2\right)\right)^2, \qquad [6]$$

where $A_0$ and $\mathcal{U}$ are phenomenological parameters reflecting the material's properties (49, 50).

The elastic contribution $f_{\mathrm{elas}}$ penalizes deviations of the nematic director field from a uniform configuration (51, 52):

$$f_{\mathrm{elas}} = \frac{1}{2}L_1\frac{\partial Q_{ij}}{\partial x_k}\frac{\partial Q_{ij}}{\partial x_k} + \frac{1}{2}L_2\frac{\partial Q_{jk}}{\partial x_k}\frac{\partial Q_{jl}}{\partial x_l} + \frac{1}{2}L_3 Q_{ij}\frac{\partial Q_{kl}}{\partial x_i}\frac{\partial Q_{ki}}{\partial x_l} + \frac{1}{2}L_6 Q_{lk}\frac{\partial Q_{ij}}{\partial x_l}\frac{\partial Q_{ij}}{\partial x_k}, \qquad [7]$$

where $L_1$, $L_2$, $L_3$, and $L_6$ are the elastic constants corresponding to the splay ($K_{11}$), twist ($K_{22}$), and blend ($K_{33}$) contributions in the Frank–Oseen free energy estimated from the elastic constant of CCN-47. The terms $L_4$ and $L_5$ are ignored here, as they describe saddle-splay and chirality, respectively.

Additional terms $f_{\mathrm{flex}}$ and $f_{\mathrm{diel}}$ account for flexoelectric and dielectric energies in the presence of an externally applied electric field. Flexoelectricity arises from the interplay of nematic distortion and polarization (53–56):

$$f_{\mathrm{flex}} = -\frac{4}{3}\chi_0 E_i\partial_j Q_{ij} - \frac{4}{3}\chi_+ E_i\left(Q_{ik}Q_{jk}\right) - \frac{1}{3}\chi_2 E_k\partial_k\left(Q_{ij}Q_{ij}\right) - \frac{4}{9}\chi_- E_i\partial_j(Q_{ik}\partial_j Q_{jk} - Q_{jk}\partial_j Q_{ik}), \qquad [8]$$

where $\chi_0$, $\chi_+$, $\chi_2$, and $\chi_-$ are material-dependent parameters.

The dielectric energy contribution is (57, 58)

$$f_{\mathrm{diel}} = -\frac{1}{2}\epsilon_0\epsilon_{ij}E_iE_j, \qquad [9]$$

with $\epsilon_0$ as the vacuum permittivity and $\epsilon_{ij}$ the tensorial dielectric permittivity of the nematic material. In the uniaxial case,

$$\epsilon_{ij} = \epsilon_\perp\delta_{ij} + \left(\epsilon_{||} - \epsilon_\perp\right)n_in_j \qquad [10]$$

Alternatively, by introducing an isotropic dielectric permittivity $\overline{\epsilon}$ and the permittivity anisotropy $\epsilon_a = \epsilon_{||} - \epsilon_\perp$, the expression can be written in terms of the **Q**-tensor:

$$f_{\mathrm{diel}} = -\frac{1}{2}\epsilon_0\epsilon_a E_iQ_{ij}E_j. \qquad [11]$$

Mixed boundary conditions are applied, including planar orientation at most surfaces, a small patch of homeotropic anchoring at the center of the top wall, and planar anchoring at the bottom. An electric field is applied along the $z$-axis, perpendicular to the surface, consistent with the negative dielectric anisotropy ($\Delta\varepsilon = \varepsilon_{\|} - \varepsilon_\perp << 0$). The director is aligned along the $x$-axis, and periodic boundary conditions are applied in the $x$- and $y$-directions.

At the confining boundaries $\partial V$ with unit normal $\boldsymbol{\nu}$, anchoring conditions are imposed by adding a surface term to the free energy:

$$\mathcal{F}_{\mathrm{surf}} = \int_{\partial V} f_{\mathrm{surf}}dS. \qquad [12]$$

Different anchoring modes (homeotropic or planar) are enforced at the droplet surface. The homeotropic anchoring is described with a Rapini–Papoular-like surface free energy density (59, 60):

$$f_{\mathrm{surf}} = \frac{1}{2}W\left(\mathbf{Q} - \mathbf{Q}^0\right)^2, \qquad [13]$$

which penalizes deviations from the preferred tensorial order parameter $\mathbf{Q}^0 = S_{\mathrm{eq}}(\boldsymbol{\nu\nu} - \mathbf{I}/3)$. The fourth-order Fournier–Galatola free energy density

$$f_{\mathrm{surf}} = \frac{1}{2}W\left(-\overline{\mathbf{Q}} - -\overline{\mathbf{Q}}_\perp\right)^2 + \frac{1}{4}W\left(-\overline{\mathbf{Q}}: -\overline{\mathbf{Q}} - S_{\mathrm{eq}}^2\right)^2, \qquad [14]$$

is used for degenerate planar anchoring, where $W$ controls the anchoring strength, $\overline{\mathbf{Q}} = \mathbf{Q} + \frac{1}{3}S_{\mathrm{eq}}\boldsymbol{\delta}$, $\overline{\mathbf{Q}}_\perp = \mathbf{p}\cdot\overline{\mathbf{Q}}\cdot\mathbf{p}$ and $\mathbf{p} = \boldsymbol{\delta} - \boldsymbol{\nu\nu}$

.

**Data, Materials, and Software Availability.** The data are available in Zenodo (61). All other data are included in the article and/or supporting information.

**ACKNOWLEDGMENTS.** The work is supported by the National Key Research and Development Program of China (No.2022YFA1405000), the National Natural Science Foundation of China (No. 62375141), the National Natural Science Foundation of China (No. 6240032604), and the Natural Science Foundation of Jiangsu Province, Major Project (No. BK20243067).

Author affiliations: [a]College of Electronic and Optical Engineering and College of Flexible Electronics (Future Technology), Nanjing University of Posts and Telecommunications, Nanjing 210023, China; [b]Pritzker School of Molecular Engineering, University of Chicago, Chicago, IL 60637; [c]National Laboratory of Solid State Microstructures, College of Engineering and Applied Sciences, and Collaborative Innovation Center of Advanced Microstructures, Nanjing University, Nanjing 210093, China; [d]Smith School of Chemical and Biomolecular Engineering, Cornell University, Ithaca, NY 14853; [e]Center for Molecular Engineering, Argonne National Laboratory, Lemont, IL 60439; and [f]Tandon School of Engineering, New York University, 70 Washington Square South, New York, NY 10012

1. S. Das *et al.*, Programming solitons in liquid crystals using surface chemistry. *Langmuir* **38**, 3575–3584 (2022).
2. O. P. Pishnyak, O. D. Lavrentovich, Electrically controlled negative refraction in a nematic liquid crystal. *Appl. Phys. Lett.* **89**, 251103–251105 (2006).
3. C. R. Rosberg *et al.*, Observation of surface gap solitons in semi-infinite waveguide arrays. *Phys. Rev. Lett.* **97**, 083901–083904 (2006).
4. Y. V. Medvedev, Collision of ion-acoustic solitary waves in plasma. *Plasma Phys. Rep.* **44**, 544–550 (2018).
5. C. Meng, J.-S. Wu, I. I. Smalyukh, Topological steering of light by nematic vortices and analogy to cosmic strings. *Nat. Mater.* **22**, 64–72 (2023).
6. Y. J. Liu *et al.*, Light-driven plasmonic color filters by overlaying photoresponsive liquid crystals on gold annular aperture arrays. *Adv. Mater.* **24**, OP131–OP135 (2012).
7. X. Liu, J. Zeng, Overcoming the snaking instability and nucleation of dark solitons in nonlinear Kerr media by spatially inhomogeneous defocusing nonlinearity. *Chaos Soliton Fract.* **156**, 111803–111809 (2022).
8. Y.-L. Li *et al.*, Tunable liquid crystal grating based holographic 3D display system with wide viewing angle and large size. *Light Sci. Appl.* **11**, 188–197 (2022).
9. L. Léger, Observation of wall motions in nematics. *Solid State Commun.* **10**, 697–700 (1972).
10. W. Helfrich, Alignment-inversion walls in nematic liquid crystals in the presence of a magnetic field. *Phys. Rev. Lett.* **21**, 1518–1521 (1968).
11. K. B. Migler, R. B. Meyer, Solitons and pattern formation in liquid crystals in a rotating magnetic field. *Phys. Rev. Lett.* **66**, 1485–1488 (1991).
12. K. B. Migler, R. B. Meyer, Spirals in liquid crystals in a rotating magnetic field. *Physica D* **71**, 412–420 (1994).
13. C. Zheng, R. B. Meyer, Structure and dynamics of solitons in a nematic liquid crystal in a rotating magnetic field. *Phys. Rev. E* **56**, 5553–5560 (1997).
14. L. Lam, Solitons in liquid crystals: Recent developments. *Chaos Solitons Fract.* **5**, 2463–2473 (1995).
15. H. R. Brand, C. Fradin, P. L. Finn, W. Pesch, P. E. Cladis, Electroconvection in nematic liquid crystals: Comparison between experimental results and the hydrodynamic model. *Phys. Lett. A* **235**, 508–514 (1997).
16. P. J. Ackerman, R. P. Trivedi, B. Senyuk, J. van de Lagemaat, I. I. Smalyukh, Two-dimensional skyrmions and other solitonic structures in confinement-frustrated chiral nematics. *Phys. Rev. E* **90**, 012505–012516 (2014).
17. H. R. O. Sohn *et al.*, Dynamics of topological solitons, knotted streamlines, and transport of cargo in liquid crystals. *Phys. Rev. E* **97**, 052701–052722 (2018).
18. B.-X. Li *et al.*, Electrically driven three-dimensional solitary waves as director bullets in nematic liquid crystals. *Nat. Commun.* **9**, 2912–2921 (2018).
19. Y. Shen, I. Dierking, Dynamics of electrically driven solitons in nematic and cholesteric liquid crystals. *Commun. Phys.* **3**, 14–22 (2020).
20. I. Nys, B. Berteloot, G. Poy, Surface stabilized topological solitons in nematic liquid crystals. *Crystals* **10**, 840–856 (2020).
21. S. Aya, F. Araoka, Kinetics of motile solitons in nematic liquid crystals. *Nat. Commun.* **11**, 3248–3257 (2020).
22. Y. Shen, I. Dierking, Dynamic dissipative solitons in nematics with positive anisotropies. *Soft Matter* **16**, 5325–5333 (2020).
23. Y. Shen, I. Dierking, Electrically driven formation and dynamics of skyrmionic solitons in chiral nematics. *Phys. Rev. Appl.* **15**, 054023–054036 (2021).
24. P. J. Ackerman, I. I. Smalyukh, Static three-dimensional topological solitons in fluid chiral ferromagnets and colloids. *Nat. Mater.* **16**, 426–432 (2017).
25. B.-X. Li, R.-L. Xiao, S. V. Shiyanovskii, O. D. Lavrentovich, Soliton-induced liquid crystal enabled electrophoresis. *Phys. Rev. Res.* **2**, 013178–013185 (2020).
26. B.-X. Li, R.-L. Xiao, S. Paladugu, S. V. Shiyanovskii, O. D. Lavrentovich, Three-dimensional solitary waves with electrically tunable direction of propagation in nematics. *Nat. Commun.* **10**, 3749–3757 (2019).
27. O. D. Lavrentovich, Design of nematic liquid crystals to control microscale dynamics. *Liq. Cryst. Rev.* **8**, 59–129 (2020).
28. S. Das *et al.*, Jetting and droplet formation driven by interfacial electrohydrodynamic effects mediated by solitons in liquid crystals. *Phys. Rev. Lett.* **131**, 098101–098106 (2023).
29. X. Wang, R. Zhang, A. Mozaffari, J. J. de Pablo, N. L. Abbott, Active motion of multiphase oil droplets: Emergent dynamics of squirmers with evolving internal structure. *Soft Matter* **17**, 2985–2993 (2021).

30. X. Tang *et al.*, Generation and propagation of flexoelectricity-induced solitons in nematic liquid crystals. *ACS Nano* **18**, 10768–10775 (2024).
31. N. Atzin *et al.*, Minimal model of solitons in nematic liquid crystals. *Phys. Rev. Lett.* **131**, 188101–188106 (2023).
32. K.-H. Wu *et al.*, Trajectory engineering of directrons in liquid crystals via photoalignment. *Soft Matter* **19**, 4483–4490 (2023).
33. H. Zhao, J.-S.B. Tai, J.-S. Wu, I. I. Smalyukh, Liquid crystal defect structures with Möbius strip topology. *Nat. Phys.* **19**, 451–459 (2023).
34. R. Voinescu, J.-S.B. Tai, I. I. Smalyukh, Hopf solitons in helical and conical backgrounds of chiral magnetic solids. *Phys. Rev. Lett.* **125**, 057201–057206 (2020).
35. J.-S.B. Tai, I. I. Smalyukh, Three-dimensional crystals of adaptive knots. *Science* **365**, 1449–1453 (2019).
36. P. J. Ackerman, I. I. Smalyukh, Diversity of knot solitons in liquid crystals manifested by linking of preimages in torons and hopfions. *Phys. Rev. X* **7**, 011006–011032 (2017).
37. C.-Y. Li *et al.*, Command of three-dimensional solitary waves via photopatterning. *Proc. Natl. Acad. Sci. U.S.A.* **121**, e2405168121–e2405168130 (2024).
38. K.-H. Wu *et al.*, Light-regulated soliton dynamics in liquid crystals. *Nat. Commun.* **15**, 7217–7227 (2024).
39. V. G. Chigrinov, V. M. Kozenkov, H. S. Kwok, *Photoalignment of Liquid Crystalline Materials* (Wiley, 2008).
40. B.-Y. Wei *et al.*, Generating switchable and reconfigurable optical vortices via photopatterning of liquid crystals. *Adv. Mater.* **26**, 1590–1595 (2014).
41. A. Martinez, H. C. Mireles, I. I. Smalyukh, Large-area optoelastic manipulation of colloidal particles in liquid crystals using photoresponsive molecular surface monolayers. *Proc. Natl. Acad. Sci. U.S.A.* **108**, 20891–20896 (2011).
42. T. Machon, G. P. Alexander, Umbilic lines in orientational order. *Phys. Rev. X* **6**, 011033–011050 (2016).
43. J. V. Selinger, Interpretation of saddle-splay and the Oseen-Frank free energy in liquid crystals. *Liq. Cryst. Rev.* **6**, 129–142 (2018).
44. J. V. Selinger, Director deformations, geometric frustration, and modulated phases in liquid crystals. *Annu. Rev. Condens. Matter Phys.* **13**, 49–71 (2022).
45. W. Wang, H. Ren, R. Zhang, Symmetry breaking of self-propelled topological defects in thin-film active chiral nematics. *Phys. Rev. Lett.* **132**, 038301–038306 (2024).
46. R. Zhang, A. Mozaffari, J. J. de Pablo, Logic operations with active topological defects. *Sci. Adv.* **8**, 9060–9067 (2022).
47. M. Yu *et al.*, Effect of biaxiality on chirality in chiral nematic liquid crystals. *Soft Matter* **14**, 6530–6536 (2018).
48. P. G. D. Gennes, J. Prost, *The Physics of Liquid Crystals* (Oxford University Press, 1993).
49. P. G. d., Gennes, Phenomenology of short-range-order effects in the isotropic phase of nematic materials. *Phys. Lett. A* **30**, 454–455 (1969).
50. P. M. Chaikin, T. C. Lubensky, *Principles of Condensed Matter Physics* (Cambridge University Press, 1995).
51. H. Mori, E. C. G. Jr., J. R. Kelly, P. J. Bos, Multidimensional director modeling using the Q tensor representation in a liquid crystal cell and its application to the π cell with patterned electrodes. *Jpn. J. Appl. Phys.* **38**, 135–146 (1999).
52. J. Nehring, A. Saupe, Calculation of the elastic constants of nematic liquid crystals. *J. Chem. Phys.* **56**, 5527–5528 (1972).
53. A. L. Alexe-ionescu, Flexoelectric polarization and second order elasticity for nematic liquid crystals. *Phys. Lett. A* **180**, 456–460 (1993).
54. L. D. Landau, E. M. Lifshitz, J. B. Sykes, J. S. Bell, E. H. Dill, *Electrodynamics of Continuous Media* (Butterworth-Heinemann, ed. 2, 1984).
55. M. L. Blow, M. M. Telo da Gama, Interfacial motion in flexo- and order-electric switching between nematic filled states. *J. Phys. Condens. Matter.* **25**, 245103–245114 (2013).
56. G. Barbero, I. Dozov, J. F. Palierne, G. Durand, Order electricity and surface orientation in nematic liquid crystals. *Phys. Rev. Lett.* **56**, 2056–2059 (1986).
57. S. P. Palto, N. J. Mottram, M. A. Osipov, Flexoelectric instability and a spontaneous chiral-symmetry breaking in a nematic liquid crystal cell with asymmetric boundary conditions. *Phys. Rev. E* **75**, 061707–061714 (2007).
58. L. A. Parry-Jones, R. B. Meyer, S. J. Elston, Mechanisms of flexoelectric switching in a zenithally bistable nematic device. *J. Appl. Phys.* **106**, 014510–014518 (2009).
59. A. Rapini, M. Papoular, Distorsion d'une lamelle nematique sous champ magnetique. *J. Phys. Colloques* **30**, 54–56 (1969).
60. M. Papoular, A. Rapini, Surface waves in nematic liquid crystals. *Solid State Commun.* **7**, 1639–1641 (1969).
61. X. Z. Tang, Reflection and refraction of directrons at the interface. Zenodo. https://doi.org/10.5281/zenodo.15544374. Deposited 29 May 2025.